Lee et al. *NPG Asia Materials* (2018) 10: 441–454
DOI 10.1038/s41427-018-0037-2

NPG Asia Materials

ARTICLE Open Access

Hydrogen adsorption engineering by intramolecular proton transfer on 2D nanosheets

Hanleem Lee[1,2], Sora Bak[3,4], Yunhee Cho[3,4], Meeree Kim[3,4], Se Hwang Kang[1,3], Viet Q. Bui[3,4], Hung M. Le[5], Sung Wng Kim[1,3] and Hyoyoung Lee[1,3,4]

Abstract

Proton transfer has been intensively researched in the catalysis of reactions involving hydrogen, such as the hydrogen evolution reaction (HER), oxygen evolution reaction, and carbon dioxide reduction. Recently, two-dimensional (2D) materials have gained attention as catalysts for these reactions, and their catalytic effect upon changing the size, shape, thickness, and phase has been studied. However, there are no reports on the role of proton transfer in catalysis by 2D materials. Here, a novel way to enhance the catalytic effect of 2D MoS_2 was demonstrated via functionalization with four different organic moieties: phenyl–Me, phenyl–OMe, phenyl–OH, and phenyl–COOH groups. The role of proton transfer in 2D catalysis was carefully investigated via electrochemical kinetic analysis and electrical measurement. The best HER performance was observed with proton-donating COOH-functionalized active materials due to intramolecular proton transfer, which shows potential in hydrogen adsorption engineering using proton transfer. In addition, other molecularly functionalized 2D catalysts, including $MoTe_2$ and graphene, also show proton transfer due to the incorporation of organic moieties, providing enhanced HER performance.

Introduction

As the world continues to develop, human activities consume an increasing amount of energy; therefore, devices for alternative energy generation have gained a great amount of interest. In particular, hydrogen has attracted attention as a renewable energy source in photocatalytic systems, environmentally friendly fuel cells[1], and water-splitting systems[2]. Proton transfer in the catalyst plays an important role in hydrogen-involved systems, including not only the hydrogen evolution reaction (HER) and hydrogen oxidation reaction but also the oxygen reduction reaction (ORR) and oxygen evolution reaction (OER). Proton transfer influences the kinetics of the HER and the oxygen reduction pathway in the ORR. For that reason, there have been numerous efforts to enhance proton transfer to obtain better catalytic effects in organometallic and solid-state catalysts[3].

Recently, two-dimensional molybdenum disulfide has been intensively studied as an electrocatalyst[4]. The 1 T phase of MoS_2 is known to be a better electrocatalyst than the 2 H phase of MoS_2 because of its faster electron transport[5]. However, the 1T phase of MoS_2 is metastable and not thermodynamically stable. This leads to degradation or phase transition of the catalyst during the HER. Therefore, a novel form of MoS_2 with both high stability and high catalytic performance, which are conflicting properties, is needed[6,7]. In a recent study, Chhowalla's group developed a new pathway to enhance the catalytic effect of MoS_2 by lowering the contact resistance, rather than modulating the surface area or the intrinsic conductivity[8]. Regardless of the type of phase or the number of edge sites, the catalytic effect of MoS_2 is strongly

Correspondence: Hyoyoung Lee (hyoyoung@skku.edu)
[1]Department of Energy Science, Sungkyunkwan University, Suwon 440-746, Korea
[2]Department of Engineering, Cambridge Graphene Center, University of Cambridge, Cambridge CB3 0FA, UK
Full list of author information is available at the end of the article

dependent on the conductivity between the electrode material and the catalyst because of their 2D characteristics, which is referred to as contact resistance. For example, 2H-MoS_2 in contact with a Au electrode through the 1T-MoS_2 (so-called metallic MoS_2) edge demonstrates enhanced HER performance similar to that of metallic MoS_2. However, fundamental studies investigating how the catalytic effect of transition metal dichalcogenide (TMD) materials is different from that of metal catalysts, especially in terms of exploiting the 2D characteristic of the materials, are lacking. Because 2D materials follow quantum physics or quantum chemistry, they have extraordinary intrinsic properties different from those of bulk materials[9]. Previously, MoS_2 nanosheets functionalized with certain organic molecules have been demonstrated to facilitate HER activity using the chemistry-sensitive physical properties of 2D materials[10]. Some researchers insist that dopants enhance the carrier concentration, which can generate a new state or increase the carrier density near the Fermi level[11]. Others suggest that the band state shifts to near the hydrogen reduction potential after doping[12,13]. However, various organic molecules show different behaviors in terms of the HER performance. For instance, p-type or chemisorption shows a higher catalytic effect than n-type or physisorption in some cases, whereas the opposite trend is found in other circumstances, indicating that previous explanations are not complete[14,15]. In-depth investigations of the mechanism of HER activity for functionalized MoS_2 and other 2D materials, such as TMDs and graphene, are insufficient. Thus, it is necessary to clarify the mechanism of HER activity for functionalized MoS_2 as well as to develop technical breakthroughs in 2D catalysis.

In this study, we focus on the enhanced catalytic effect of functionalized MoS_2 with an emphasis on the proton transfer mechanism. To minimize the complexity of the factors influencing the catalytic effect, we initially investigate the fundamental catalytic effect of functionalized MoS_2 depending on the size, number of layers, and doping. Then, the catalytic enhancement of functionalized MoS_2 through intramolecular proton transfer, particularly in the HER, is introduced. The functionalization of 2D materials is one of the easiest ways to develop new functionality in TMD materials while maintaining the original intrinsic properties (e.g., electrical behavior)[11]. To introduce various new organic molecular functionalities, para-substituted benzene diazonium salts, which are able to incorporate various substituents, were chosen to modify MoS_2. Interestingly, carboxyl (COOH)-functionalized MoS_2 shows a lower Tafel slope of approximately 56 mV per decade, which is associated with a change in the rate-determining step from adsorption to desorption. This is because the COOH moiety increases the polarization of the electrode, which is related to wettability, as well as reduces the hydrogen absorption energy of the Mo and S atoms through proton transfer[16], thus converting low-activity Mo or S to high-activity Mo or S for the HER.

Experimental procedure

Thin-film working electrode

PET substrates were cleaned with warm isopropyl alcohol, and O_2 plasma treatment was subsequently performed. PDMS mixtures (silicone elastomer base:silicone elastomer curing agent = 10:1 volume ratio) were spin-coated at 500 rpm for 30 s, 3000 rpm for 12 s, 5000 rpm for 10 s, and 300 rpm for 5 s onto the PET substrates after standing for 30 min and were then cured at 90 °C overnight. Next, 50 nm of Au was deposited on PDMS/PET as the conductor electrode. A f-MoS_2 solution was prepared based on a previous paper[15]. Details of the preparation of f-MoS_2 and e-MoS_2 are given in the Supporting Information. Then, 2 mg/ml of f-MoS_2 was diluted with triple-distilled water to engineer the surface energy between the droplet and the substrate during coating. The solvent (DMF:H_2O) ratio was adjusted to 1:1 in the final f-MoS_2 suspension, resulting in a 1 mg/ml concentration. Then, f-MoS_2 was spray-coated onto the Au/PDMS substrate. The e-MoS_2 electrode was prepared using the same procedure as that for f-MoS_2.

Measurement of the electrochemical and other physical properties

A 920 C SECM (CH Instruments, TX, USA) was used for the electrochemical measurement. The working electrode was placed between a Pt wire counter electrode and a Ag/AgCl (saturated KCl) reference electrode. All potentials given in this work were calculated against the Ag/AgCl reference electrode (0.197 eV). All electrochemical measurements were performed in 0.5 M H_2SO_4 aqueous solution with H_2 purging, except during the pH test. pH measurements were conducted in phosphate buffer solution using H_2SO_4 to adjust to the desired pH. Raman spectroscopy (inVia™ confocal Raman microscope, Renishaw), XPS (ESCA 2000, VG Microtech, Netherlands), and AFM (SPA 3800, Seiko, Japan) were used for surface characterization.

Measurement of the electrical properties

The source–drain current versus voltage was measured by a 4200 Keithley semiconductor characterization system at room temperature in a vacuum of $1 \times 10^{-4} - 1 \times 10^{-5}$ torr. The film was fabricated by the spin-coating method on a 50 nm Au electrode on a SiO_2/Si substrate. The width of the source and drain electrodes was 50 μm, and the length of the channel was 100 μm.

Results

Fundamental factors in the catalysis of 2D materials

Figure S1 presents a schematic illustration of the experimental process used to fabricate functionalized MoS_2. To exclude other factors that might affect the catalytic effect of TMD materials, we first determined the HER performance with different doping levels and different thicknesses. We fabricated a film-type HER working electrode with a uniform morphology as the catalyst. Au is used as both a conductor to allow for electron transfer in the film-type working electrode and as a p-type dopant in MoS_2 to shift the conduction band (CB) of MoS_2 toward the hydrogen reduction potential; this is done because the work function of Au and the valence band of MoS_2 have similar band levels (ϕ_{Au} = 5.2 eV, VB = 5.4 eV). Unlike bulk TMD materials, the electronic structure of nano-dimensional TMDs has been reported to have a strong relationship with the substrate due to the screening effect[17]. Although Au nanoparticles themselves have a good catalytic effect on the HER, we suggest that the HER performance predominately originates from MoS_2 because the electrode is fully covered with MoS_2 (in our system, some MoS_2 experiments present a lower catalytic effect than the Au electrode). The polarization curves of the current density–potential characteristics show differences for different doping levels and number of layers. The reduced onset potential with an increased doping level is due to the band state modulation, which was confirmed by core-band and valence-band X-ray photoelectron spectroscopy (XPS). Edge functionalization of MoS_2 (e-MoS_2) with different doping levels was explored in our previous research, so we followed the procedure described in that paper[18]. We named the sample monolayer Cx_e-MoS_2, where Cx represents the number of alkyl chains of the alkyl amine, which plays an important role in controlling the reactivity of diazotization for edge functionalization. In particular, an alkyl amine with a longer chain effectively extends the d-spacing of MoS_2 and changes the polarizability of MoS_2, leading to a higher edge doping level (Figure S4). Figure S2b shows that the Fermi level proportionally downshifts in the order of monolayer C2_e-MoS_2 < monolayer C4_e-MoS_2 < monolayer C10_e-MoS_2 due to the higher edge doping levels, which are 0.084 eV for f(COOH)–MoS_2, 0.93 eV for C10_e-MoS_2, 1.79 eV for C4_e-MoS_2, and 1.67 eV for C2_e-MoS_2. Fully functionalized f(COOH)–MoS_2 using the same diazonium salt dopant was also investigated as a control. Through p-type doping of COOH, the CB of the edge-functionalized MoS_2 approaches the hydrogen reduction potential and provides an improved catalytic effect[19]. 2H-MoS_2 was made by a solvent exfoliation method, and this material dominantly conforms to a multilayer structure. The onset of the HER activity of 2H-MoS_2 was near −220 mV vs. the reversible hydrogen electrode (RHE), and the onset shifts to a lower overpotential as the edge functionalization region increases

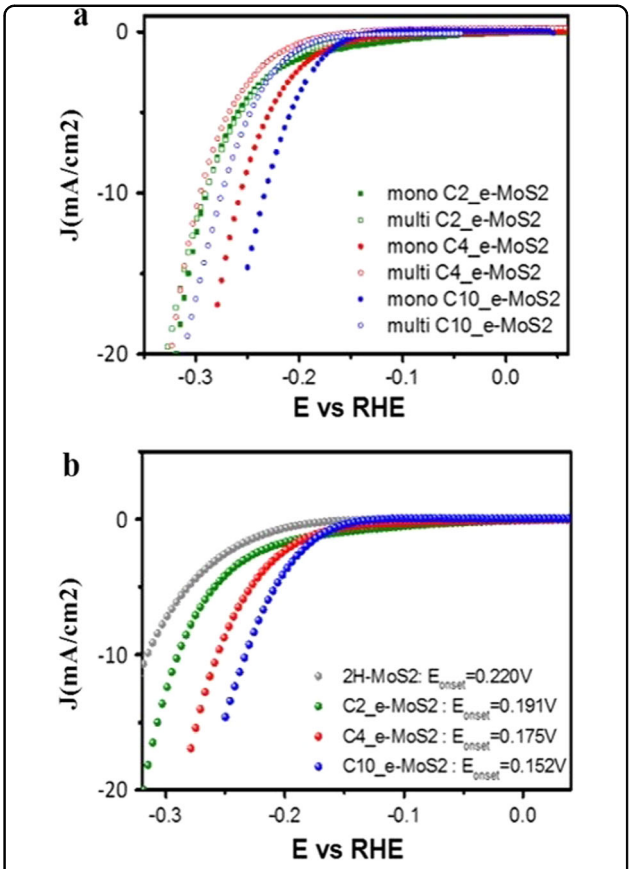

Fig. 1 Doping effect on the HER: a HER properties at different doping levels and with different numbers of layers. The J–V curve demonstrates a higher onset potential for multilayer e-MoS_2 than for monolayer e-MoS_2. **b** J–V curves of e-MoS_2 with different edge doping levels

(E_{onset}^{C2} = 191 mV, E_{onset}^{C4} = 175 mV, E_{onset}^{C10} = 152 mV) with a monolayer of e-MoS_2 (Fig. 1). The thickness also affects the onset potential by changing the effective surface area and the band state[20,21]. The number of layers depends on the purification process and can be directly investigated by the difference in the E_{2g} and A_{1g} peaks in the Raman spectrum[22] (Figure S2a). Multilayer e-MoS_2 produced by C2, C4, and C10 does not exhibit a good linear tendency like monolayer Cx_e-MoS_2, but its onset potential is lower than that of 2H-MoS_2 and slightly higher than that of monolayer e-MoS_2 (approximately 210 mV, Fig. 1b). We speculate that the increased edge exposure in the monolayer samples leads to thermodynamically favorable electrocatalytic activity, and their narrower distribution of electronic properties demonstrates the clearly enhanced HER upon doping over that of multilayer samples[21]. Thus, we fabricated working electrodes using functionalized monolayer MoS_2 (f-MoS_2) with similar doping levels, as confirmed by AFM (Figure S9–10).

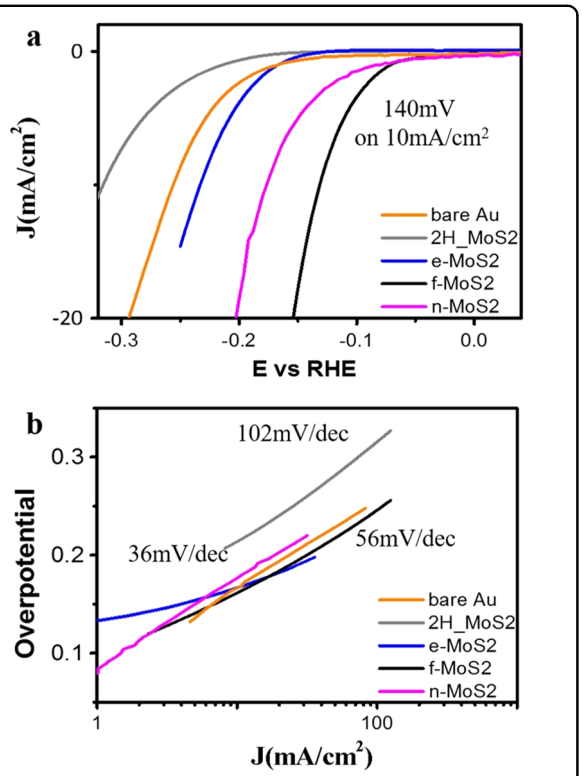

Fig. 2 HER performance of f-MoS_2: **a** J–V curves and **b** corresponding Tafel plots for bare Au, 2H-MoS_2, edge-functionalized MoS_2 (e-MoS_2), fully functionalized MoS_2 (f-MoS_2), and metallic MoS_2 (n-MoS_2). The curves show the cathodic sweep of the second cycle

Then, we estimated the catalytic activity depending on the doping position, where e-MoS_2 represents monolayer C10_e-MoS_2. The e-MoS_2 demonstrates a dramatically improved exchange current and onset potential (230 mV vs. RHE for 10 mA/cm^2) compared to 2H-MoS_2 (310 mV vs. RHE for 10 mA/cm^2) or the Au electrode (265 mV vs. RHE for 10 mA/cm^2), as shown in Fig. 2. This means that H adsorption at the COOH doping site is closer to equilibrium than it is at the common edge site[23]. Full functionalization of MoS_2 (functionalization on both the basal plane and edge site, f-MoS_2) further enhances the HER performance because new active sites, such as defects and functional groups, are generated. As a result, f(COOH)–MoS_2 shows the smallest onset and largest exchange current, which are even higher than those of metallic MoS_2 (n-MoS_2), although the intrinsic resistance of f(COOH)–MoS_2 is higher than that of n-MoS_2 (Fig. 3c). In addition, f(COOH)–MoS_2 is more stable than n-MoS_2 (Figure S3), which is believed to originate from the functional groups stabilizing the defect sites of MoS_2. The XPS spectra in Figure S5 show that the 2H/1T ratio estimated at the Mo 3*d* 3/2 orbital before and after HER test is not significantly different for f(COOH)–MoS_2 (from 3.01 to 2.97), but a large change is observed for n-MoS_2 (from 0.97 to 1.24). In addition, after 1000 HER cycles, n-MoS_2 exhibits a large proportion of the Mo^{6+} state at 234 eV and 236 eV, which is the oxidized form of Mo. Amazingly, no such states are observed in f(COOH)–MoS_2 after 1000 HER cycles because the COOH sites, surrounded by defects or neighboring layers, bring structural stability to the system[24].

Molecularly functionalized ligand effect

To determine the factors that enhance the catalytic effect of f-MoS_2, we synthesized four different f-MoS_2 sheets with four different functional groups: phenyl–COOH, phenyl–CH_3(ME), phenyl–OCH_3(OME), and phenyl–OH. Two of these are p-type dopants (phenyl–COOH and phenyl–ME), and two are n-type dopants (phenyl–OME and phenyl–OH)[25]. Their functionalization with MoS_2 was confirmed by IR and Raman spectroscopy (Figure S6–S7). Peaks corresponding to aromatic C = C bonds are observed at approximately 1400 and 1600 cm^{-1}, and a S–C bonding peak is observed at 680 cm^{-1} for all four f-MoS_2 samples, representing functionalization at the S site. Additionally, the peaks are slightly shifted, indicating the influence of the chemisorbed functional groups[26]. Band modulation can also be verified by investigating the Raman shifts. Due to the different band state positions corresponding to the E_{2g} and A_{1g} vibrational modes of bare MoS_2, f-MoS_2 demonstrates different types of band shifts. The OME and OH groups, which are strong electron-donating functional groups, show a redshift because of the upshift of the band state. Alternatively, COOH is a weak electron-donating functional group, and ME is a strong electron-withdrawing group, which produce a blueshift because of the downshift of the band state[27,28]. The PL and PLE spectra agree with these results as well as the different band state changes depending on the organic dopant (Figure S8). Interestingly, independent of the band modulation, functional groups with a weak hydrogen binding energy (e.g., COOH and OH groups) enhanced the HER performance. f(COOH)–MoS_2, f(OH)–MoS_2, f(ME)–MoS_2, and f(OME)–MoS_2 show an onset of HER activity near −101, −105, −147, and −142 mV vs. RHE, respectively, as can be observed in Fig. 4a. The onset of the catalytic activity shifts to a lower overpotential when the binding energy of hydrogen in the functional groups decreases, which is related to the proton transfer behavior (i.e., the ligand effect).

First, we compared the conductivity of the various functionalized samples because the conductivity is known to increase the catalytic effect of f-MoS_2. Interestingly, the polarization curves of f-MoS_2 indicate good performance when only a small amount of f-MoS_2 is deposited (Fig. 3a). This indicates that the characteristics of the 2D material

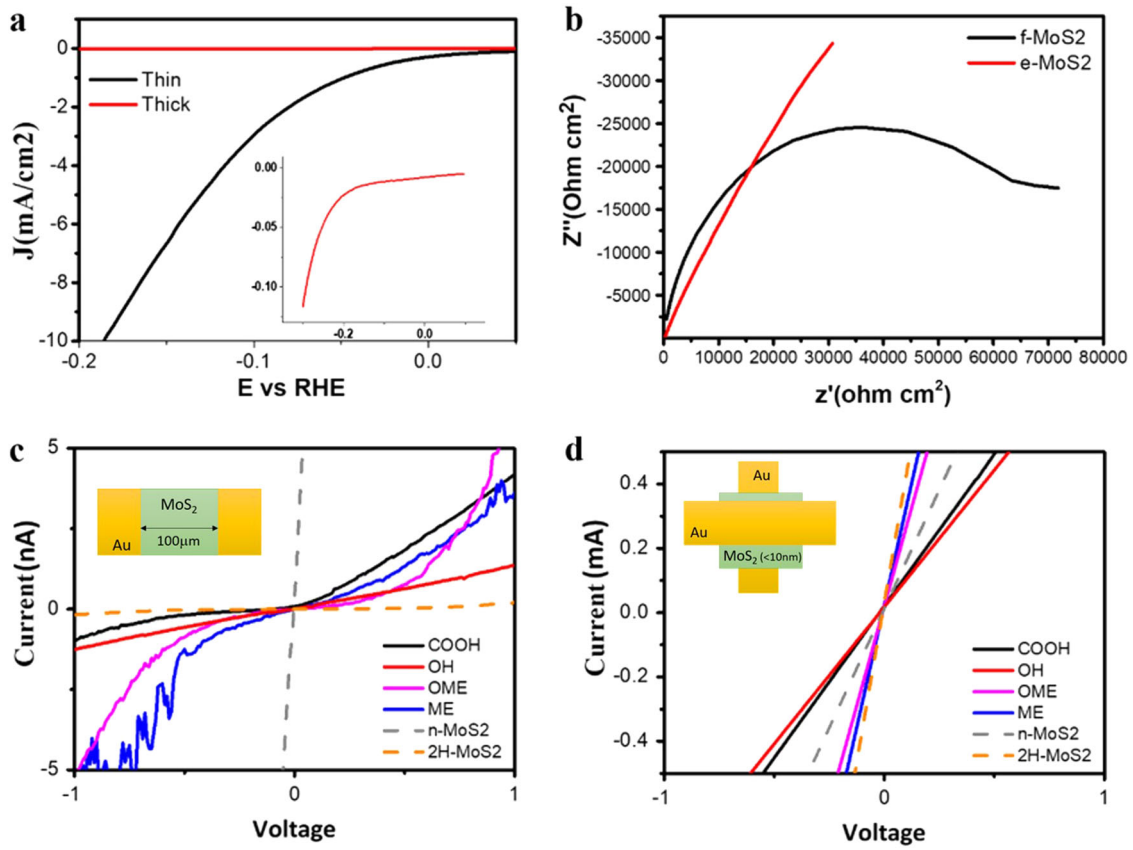

Fig. 3 Conductivity effect: a Polarization curves depending on the amount of catalyst. Small amounts of f-MoS_2 and large amounts of f-MoS_2 are observed through electrochemical measurements. The inset is the magnified figure of the J–V curve for thick f-MoS_2. **b** EIS spectra of thick-film f-MoS_2 and e-MoS_2. Both MoS_2 samples demonstrate large electron transport resistance. **c** I–V curves of the in-plane conductivity of f-MoS_2 with COOH, OH, OME, and ME functional groups; metallic n-MoS_2; and 2H-MoS_2. **d** I–V curves of the out-of-plane conductivity of f-MoS_2 with COOH, OH, OME, and ME functional groups; metallic n-MoS_2; and 2H-MoS_2

(e.g., functional group, proton transfer, wettability and band state), rather than the conductivity change, strongly affect the HER performance of the 2D material when the thickness of the catalyst film on the electrode is less than ten nanometers. Electrons ejected from the electrode can move along a several-nanometer-thick film through the tunneling effect or hopping transport[8], but cannot with a thick film. As a result, a thin film of the f-MoS_2 catalyst shows good HER performance and high current despite the low conductivity of the material, while a thick f-MoS_2 layer demonstrates a sharp decline in the HER performance due to the strong influence of conductivity. The I–V curves support these results (Fig. 3c, d). The in-plane conductivity of all four f-MoS_2 samples, which is related to the intrinsic conductivity, shows a small increase over that of 2H-MoS_2 (Fig. 3c). However, the in-plane conductivities of the f-MoS_2 samples did not changed significantly, and all samples show semiconductor behavior: the metallic n-MoS_2 shows a current level of 10^{-6} that leads to 5×10^6 ohm and f-MoS_2 demonstrates a current level of 10^{-9} that leads to approximately 10^9 ohm. This is because f-MoS_2 still exhibits semiconductor behavior, unlike metallic MoS_2, leading to the semi-circle impedance plot and a large electron transport impedance for the thick film[29] (Fig. 3b). On the other hand, the I–V curves of vertical devices of all four f-MoS_2 ($t < 10$ nm) samples reveal a current level of 10^{-4}, which is similar to that of metallic n-MoS_2 and 2H-MoS_2 ($t < 10$ nm, Fig. 3d). We measured the out-of-plane conductivity of the three f(COOH)–MoS_2 samples, and even though the out-of-plane conductivity is different among the samples (0.2 mA), their onset potentials are similar (±10 mV), as shown in Figure S11. Thus, the out-of-plane conductivity of f-MoS_2 does not have a dominant effect on the HER performance for the several-nanometer catalyst film, meaning the different onset potential and current density of the HER performance, depending on the organic functional group, was not derived from the conductivity but from the ligand effect (band state modulation and proton transfer).

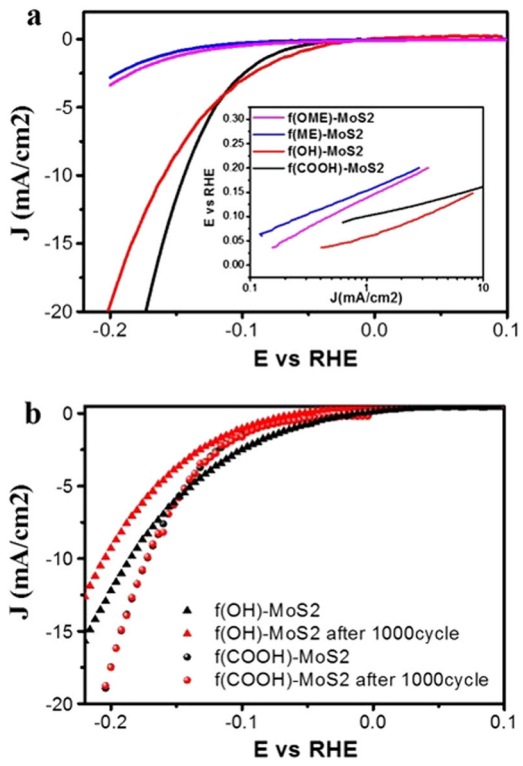

Fig. 4 a J–V curves for fully functionalized MoS_2 (f-MoS_2) with different functional groups (f(COOH)–MoS_2, f(OH)–MoS_2, f(ME)–MoS_2, and f(OME)–MoS_2). The inset shows the corresponding Tafel slopes of **a**. **b** Stability tests for f(COOH)–MoS_2 and f(OH)–MoS_2 before and after 1000 HER cycles

In addition, the ligand effect can be interpreted through investigation of the kinetics. The rate-determining step in the 2H-MoS_2 HER reaction is the adsorption of hydrogen, rather than the desorption, and so proper bonding with H at an active site kinetically enhances the electrocatalytic activity[30]. In our experiment, e-MoS_2 shows a lower Tafel slope but a higher onset potential than f-MoS_2 (Fig. 2b). This is because f-MoS_2 shows thermodynamically improved catalytic activity due to the large number of effective active catalytic sites and defects near the functionalized organic moiety, even though e-MoS_2 shows kinetically improved catalytic activity[31]. The kinetically improved catalytic activity of e-MoS_2, compared to f-MoS_2, is caused by the higher activity of the edges of the functionalized MoS_2 due to the lower H binding energy compared to that of the functionalized basal plane, as supported by our discrete Fourier transform (DFT) calculations (Fig. 5). The various functionalized MoS_2 nanosheets provide different electrocatalytic activities. The f(COOH)–MoS_2 nanosheets exhibit the lowest overpotential and lowest Tafel slope, while f(OH)–MoS_2 displays low overpotential and high Tafel slope. The f(ME)–MoS_2 and f(OME)–MoS_2 samples show high overpotential and high Tafel slope. Moreover, f(OH)–MoS_2 exhibits electrocatalytic losses in the J–V curve after 1000 HER cycles because of the structural instability of the functional groups after the hydrogen shift (Fig. 4b). In contrast, f(COOH)–MoS_2 does not show significant changes. Unlike the HER performance of 2H-MoS_2, which follows the adsorption-dependent Volmer–Tafel mechanism, f(COOH)–MoS_2 is considered to follow the desorption-dependent Volmer–Heyrovsky or Volmer–Tafel–Heyrovsky mechanism, which agrees with the values of the Tafel slope (approximately 56 mV per decade)[32] shown in Fig. 4a. The other functional groups of f(OH)–MoS_2, f(ME)–MoS_2, and f(OME)–MoS_2 do not follow desorption-dependent behavior. The Tafel slopes for f(OH)–MoS_2, f(ME)–MoS_2, and f(OME)–MoS_2 are 89, 98, and 121 mV per decade, respectively (inset of Fig. 4a). The exchange current density, shown in Fig. 6a, of f(COOH)–MoS_2 and f(OH)–MoS_2 is dramatically enhanced over that of f(ME)–MoS_2 and f(OME)–MoS_2, showing a similar trend as that of the overpotential. As mentioned previously, the larger number of effective active sites directly leads to a reduction in the overpotential of all four f-MoS_2 compared to 2H-MoS_2. We then asked why OH and COOH substituents produce a larger number of effective active sites than ME or OME. Wettability, or the polarizability of the electrode, is the dominant reason. The wettabilities of f(COOH)–MoS_2, f(OH)–MoS_2, f(ME)–MoS_2, and f(OME)–MoS_2 were investigated *via* changes in their electrical properties (Fig. 7c). f(COOH)–MoS_2 and f(OH)–MoS_2 show large current suppression at a negative bias voltage, while f(COOH)–MoS_2 presents a significantly low current at a positive bias voltage. The current drop is associated with the strong interaction between water molecules and the functionalized MoS_2. When the wettability of the functionalized MoS_2 increases, the current drop also increases due to the high degree of scattering induced by water molecules.

Consequently, f(COOH)–MoS_2 and f(OH)–MoS_2 show high wettability with water, which is beneficial for the HER reaction. Furthermore, pH-dependent LSV curves were measured to provide evidence of the ligand effect on MoS_2 (Fig. 6b). The onset potential and exchange current are dramatically affected by the pH of the solution[16] according to the Nernst Equation, but this tendency is not accurately followed when the electrode has poor polarizability. Thus, an electrode with good wettability exhibits a shift in the reaction potential of approximately 57 mV with a pH increase of 1. In our experiment, f(OH)–MoS_2 shows a lower activity shift (0.201 V) in both the exchange current and the onset potential, even though f(COOH)–MoS_2 demonstrates a higher activity shift (depending on the pH, 0.252 V), and the degree of the

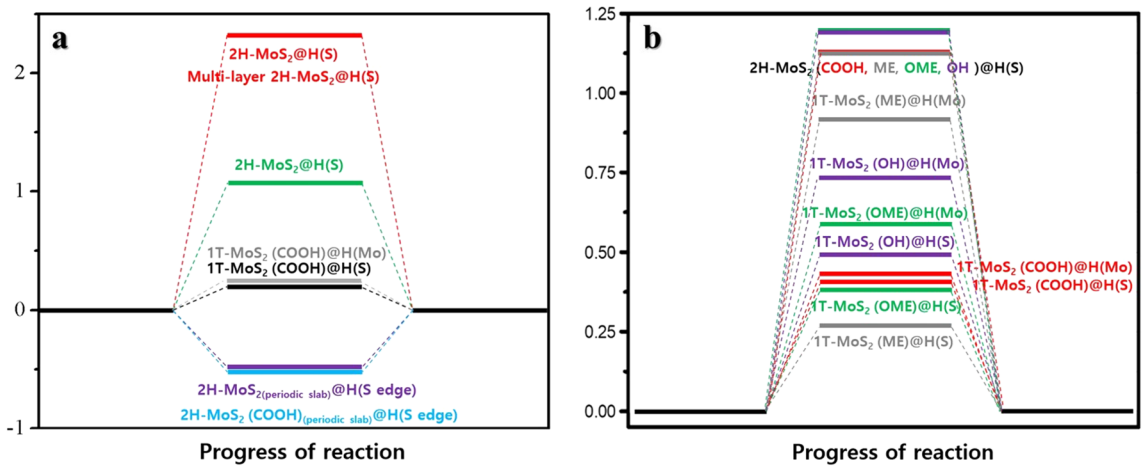

Fig. 5 DFT calculations: a Comparison of ΔG_H at various H bonding sites (Mo atom, S atom, and S edge) on monolayer 2H–MoS_2, multilayer 2H–MoS_2, and f(COOH)–MoS_2. **b** Comparison of ΔG_H at various H bonding sites for MoS_2 samples functionalized with COOH (red), OH (purple), ME (gray), and OME (green)

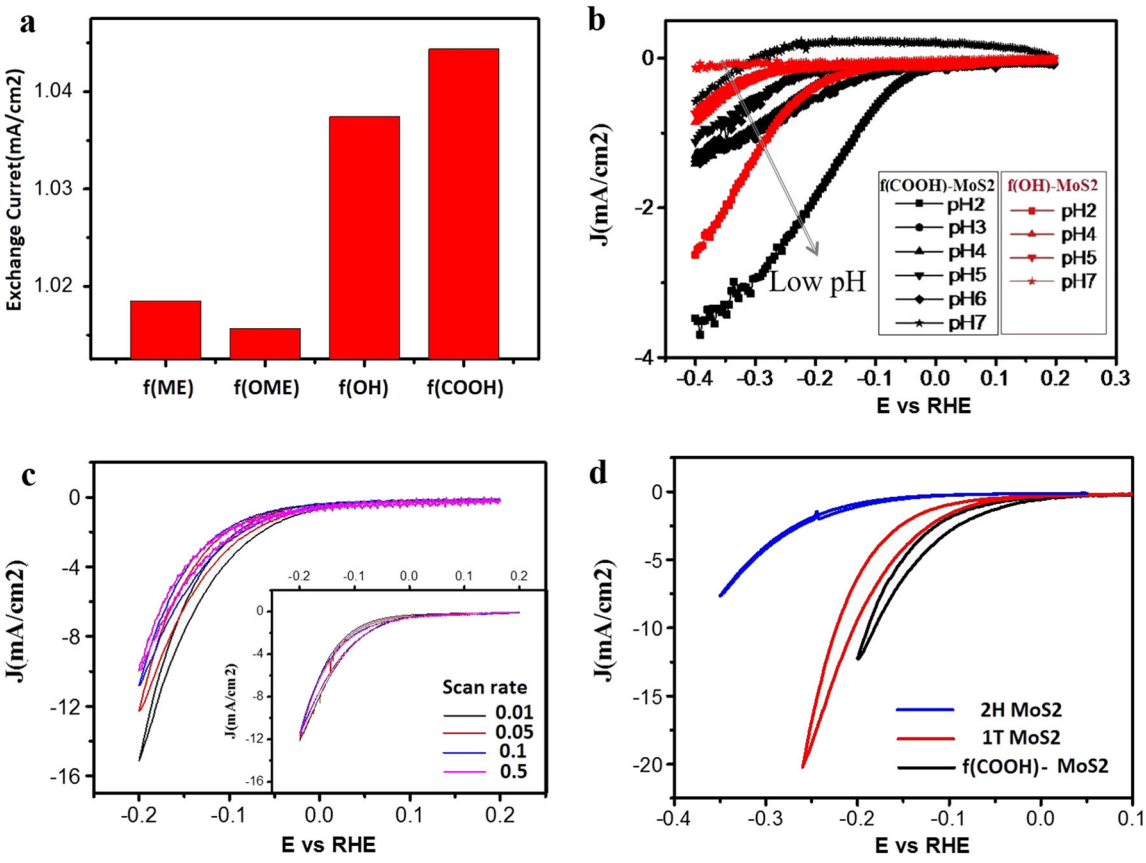

Fig. 6 Kinetic analysis: a Exchange current of molecularly functionalized MoS_2. **b** Voltammograms of COOH-functionalized MoS_2 in phosphate buffer with the pH adjusted to 2, 3, 4, 5, 6, and 7 by H_2SO_4 (black) and voltammograms of OH-functionalized MoS_2 in phosphate buffer with the pH adjusted to 2, 4, 5, and 7 by H_2SO_4 (red). **c** C–V characteristics of f(COOH)–MoS_2 at different scan rates. The inset denotes the C–V characteristics of f (ME)–MoS_2 at different scan rates. **d** C–V characteristics of 2H-MoS_2, f(COOH)–MoS_2, and 1T MoS_2

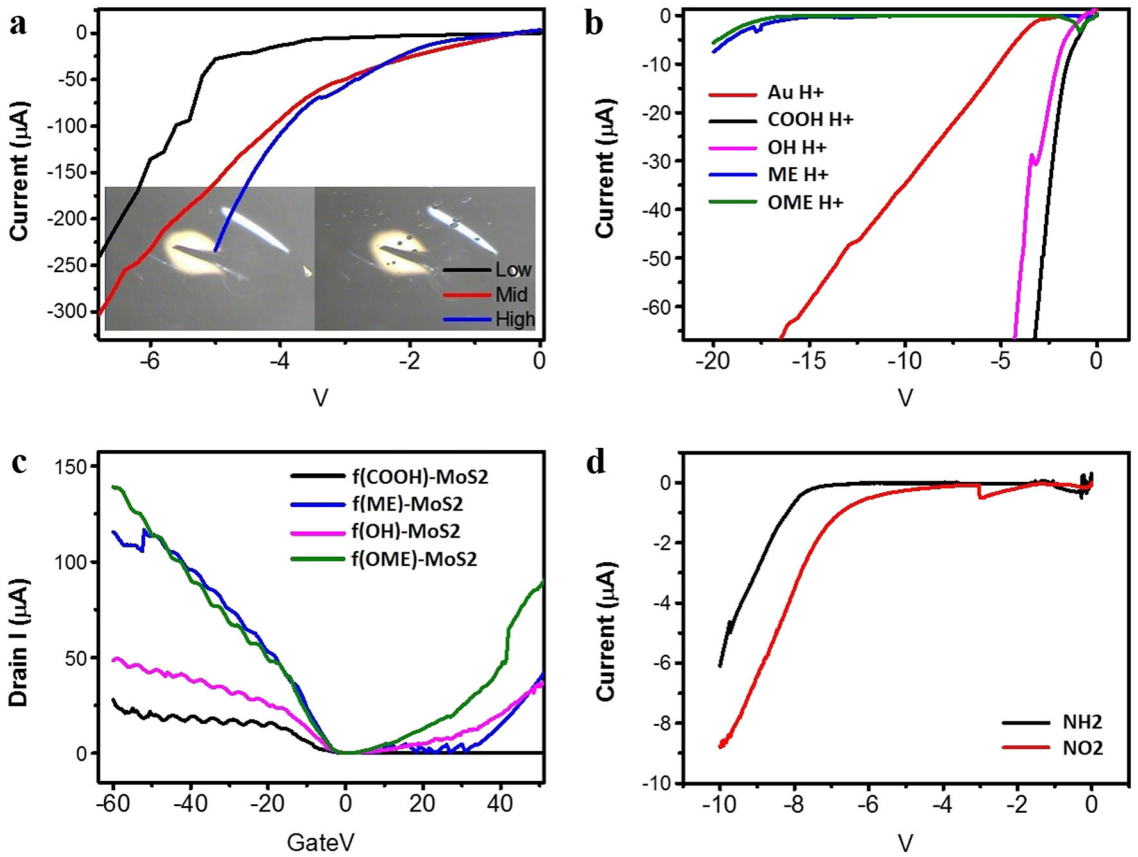

Fig. 7 Electrocatalytic effects of organic functional groups: a I–V curves of COOH-functionalized Au electrodes with respect to the density of the organic molecules. **b** I–V curves of a Au and diazonium salt-functionalized Au electrode in 0.5 M H_2SO_4. **c** Transfer curves of functionalized MoS_2 flakes during H_2O adsorption. **d** I–V curves of NH_2 and NO_2-functionalized Au electrodes in 0.5 M H_2SO_4

activity shift from pH 2 to pH 7 is much closer to the theoretical value (0.28 V). However, the different pH dependencies of the catalytic effect are larger than expected since f(OH)–MoS_2 shows comparable wettability. We believe that the carboxyl moiety serves as a proton shuttle in our system, which leads to the significant enhancement in the HER performance.

$$\begin{aligned} &HOOC-S-Mo^{4+}-\text{vacancy} \leftrightarrow {}^{-}OOC \\ &-S-Mo^{4+}-H \rightarrow HOOC-S-Mo^{4+}-H \end{aligned} \quad (1)$$

$$\begin{aligned} &HOOC-S-Mo^{4+}-H \rightarrow^{-} OOC-S-Mo^{4+}-H_2 \\ &\rightarrow HOOC-S-Mo^{4+}-\text{vacancy}+H_2 \end{aligned} \quad (2)$$

$$\begin{aligned} &HOOC-S-Mo-S \leftrightarrow^{-} OOC-S-Mo \\ &-SH(\text{delocalization}) \rightarrow HOOC-S-Mo-SH \end{aligned} \quad (3)$$

$$\begin{aligned} &HOOC-S-Mo-SH \leftrightarrow^{-} OOC-S-Mo-S \\ &-H_2 \rightarrow HOOC-S-Mo-S+H_2 \end{aligned} \quad (4)$$

The basic mechanism of the HER with f(COOH)–MoS_2 is similar to that of common MoS_2 using a vacancy site as the active site. The main difference is that intramolecular proton transfer facilitates hydrogen adsorption[16]. Rapid intramolecular proton transfer from the carboxyl compensates for the activity of hydrogen adsorption and desorption through the above four pathways. In particular, the first hydrogen adsorption is caused by intramolecular proton transfer from the organic COOH functional group. The high electronegativity of the metal atom affects the organic moiety so that a proton on the organic COOH substitute is shifted toward the metal component at a vacancy site or a sulfide atom. Intramolecular proton transfer eventually lowers the H adsorption energy and facilitates hydrogen gas evolution. Thus, the H dissociation energy of the functional group emerges as an indicator for possible intramolecular proton transfer. Because H dissociation from the organic moiety is affected by the pH, the pH of the solution has a strong effect on the intramolecular proton transfer. In that manner, the LSV curves of f(COOH)–MoS_2 show a relatively high overpotential shift and current density shift, especially in

low pH environments since COOH is a better hydrogen leaving group in acidic conditions than the OH, ME, and OME groups[33]. The finding that the C–V curves are influenced by the scan rate provides further evidence that intramolecular proton transfer is involved in the HER of f(COOH)–MoS_2 (Fig. 6c). The HER activity can be detected by the dramatic increase in current at negative potential. Generally, secondary hydrogen adsorption hardly occurs at fast scan rates. As a result, the current increase or onset potential of the HER response can be suppressed at higher scan rates[34]. The catalytic activity of f(COOH)–MoS_2 clearly depends on the scan rate, but this is not the case for f(ME)–MoS_2 (insets of Fig. 6c and S12). The difference in current density around the hydrogen absorption peak indicates that f(COOH)–MoS_2 shows a higher capacitance than 2H-MoS_2 and a lower capacitance than 1T-MoS_2, which is a result of the effective hydrogen adsorption and desorption engineering through organic functionalization (Fig. 6d). When the intermediate state is the same, a high capacitance is needed for better hydrogen adsorption in adsorption-dependent HER, while a low capacitance is better for hydrogen desorption in desorption-dependent HER.

DFT calculation

All calculations were performed *via* DFT[35,36] using the Vienna Ab-initio Simulation Package.[37,38] The interactions between the atomic cores and the electrons were described using the projector augmented wave method.[39] The generalized gradient approximation in the Perdew–Burke–Ernzerhof (PBE)[40] form was used as the electron exchange-correlation functional, along with the van der Waals correction at the Grimme-D3 level.[41] The wavefunctions were expanded using plane waves with a cutoff energy of 400 eV, the force convergence criterion was set to 0.01 eV/Å, and the total energy was smaller than 0.0001 eV/cell. The $(4 \times 4 \times 1)$ supercell and (3×3) ribbon of MoS_2 were chosen to consider basal plane and edge ligand functionalization on the 2H–MoS_2 and 1T-MoS_2 surfaces, respectively. A *k*-point grid was employed for periodic and slab-periodic calculations of sizes $(6 \times 6 \times 1)$ and $(6 \times 1 \times 1)$, respectively. A vacuum region of 17 Å was used to avoid interactions between two periodic images.

To analyze the favorability of H bonding to the functionalized MoS_2 surface, we calculated the Gibbs free energy of the reaction using the following formula:

$$\Delta G_H = \Delta E_H + \Delta E_{ZPE} - T\Delta S_H \quad (5)$$

In the above equation, ΔE_H (binding energy of H attachment) is calculated by taking the total energy of the product side (functionalized MoS_2 with H) and subtracting the total energies of the reactants (functionalized MoS_2 layer and $1/2H_2$). The difference in the zero-point vibrational energies of the product and reactant sides (ΔE_{ZPE}) is insignificant (~0.06 eV); ΔS_H is approximately half of the entropy of H_2 gas, and T was chosen as 300 K (the contribution is approximately 0.2 eV). As a result, we can simplify Eq. (5) by adding 0.26 eV to ΔE_H.[42,43] We first analyzed the attachment of H to the S site in a pure MoS_2 surface. For monolayer 2H–MoS_2, ΔG_H is reported to be 2.13 eV, which indicates that H attachment on 2H–MoS_2 is non-spontaneous. In addition, we also considered the attachment of H to the multilayer 2H–MoS_2 system, and the obtained ΔG_H is 2.15 eV, which is slightly higher than the previous case. For convenience, we summarize all ΔG_H terms investigated in this study in Fig. 5 and Table S1. The results demonstrate the same trends as found with our HER reaction experiments; multilayer MoS_2 has a higher hydrogen evolution energy than monolayer MoS_2, and basal plane functionalization gives a higher hydrogen evolution energy than edge functionalization. In particular, the edge sulfurs undergo a desorption-dependent hydrogen evolution mechanism, unlike sulfurs in the basal plane, which follow an absorption-dependent hydrogen evolution mechanism. In the next stage, we considered H attachment on 2H–MoS_2 layers functionalized with various groups (phenyl–COOH, phenyl–ME, phenyl–OME, and phenyl–OH). There are two possible attachment positions for H near the functionalized site, i.e., H can directly bind to the vacant Mo site or the neighboring S site, as indicated in Figure S13. To clarify the binding mechanism, we analyzed the Gibbs free energy of H attachment for both binding positions with respect to each functional group. For the Mo–H bond to be established, the required ΔG_H falls in the range of 2.31–2.34 eV (see Table 1 for details of each case), which is higher than that for H attachment to the S site in pure MoS_2. Such results can be understood in terms of thermodynamic stability because it is difficult for H to approach the inner Mo cation. On the other hand, bond formation between H and one neighboring S anion near the functionalized site is shown to be more favorable due to the lower positive ΔG_H values (1.12–1.19 eV). Among the four cases, our results indicate that S–H bond formation in the phenyl–COOH and phenyl-ME functionalized samples gives the lowest positive ΔG_H value (1.13 and 1.12 eV, respectively). Subsequently, we considered H attachment on the functionalized 1T phase with a change in the original phase to the 1T phase. As indicated in Table 1, H still prefers to form bonds with the S atoms (the ΔG_H quantities are lower than those for the Mo–H bond). It is observed that –COOH functionalization provides the lowest ΔG_H for Mo–H binding (0.44 eV), and a similar ΔG_H is observed for S–H binding (0.41 eV) with regard to other ligand functionalization cases, resulting in a low onset potential and low Tafel slope. Through analysis of the ΔG_H values, we can arrive

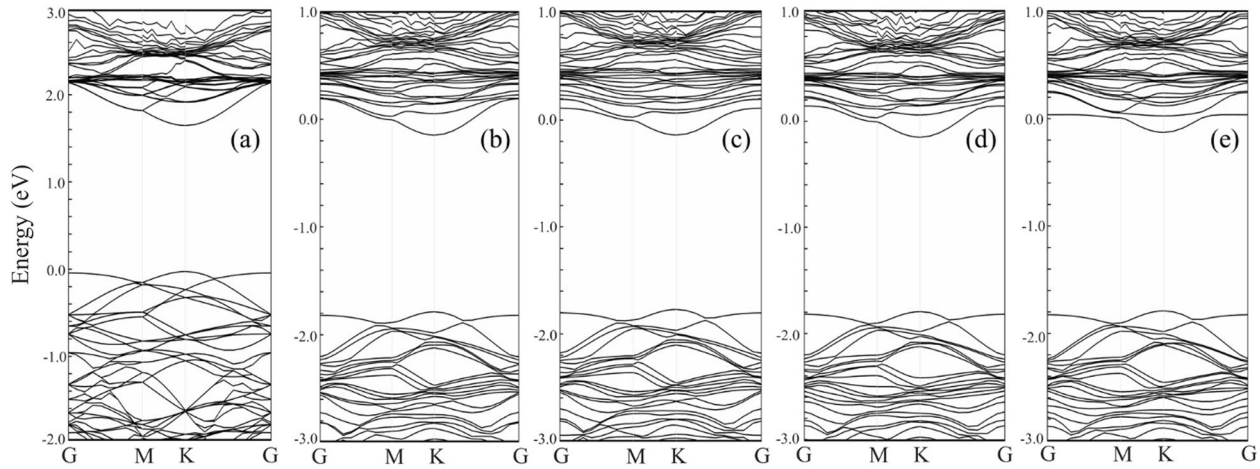

Fig. 8 Band structure of **a** a 2H–MoS_2 monolayer and the 2H–MoS_2 surface functionalized with **b** –$C_6H_4CH_3$, **c** –C_6H_4COOH, **d** –$C_6H_4OCH_3$, and **e** –C_6H_4OH groups

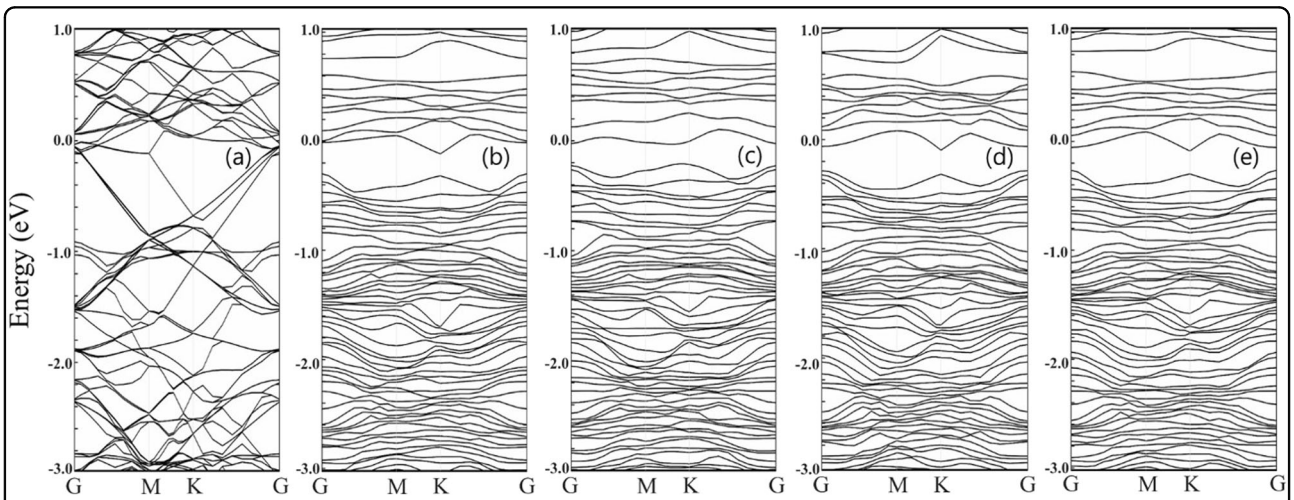

Fig. 9 Band structure of **a** a 1T–MoS_2 monolayer and the 1T MoS_2 surface functionalized with **b** –$C_6H_4CH_3$, **c** –C_6H_4COOH, **d** –$C_6H_4OCH_3$, and **e** –C_6H_4OH groups

at an important conclusion: H prefers establishing bonds with S sites neighboring the functionalized position. This result for ΔG_H is consistent with our electronic structure analysis, in which we examined the resultant band structures of the four functionalized systems (see Fig. 8). In Fig. 8, we can clearly observe that the attachment of functional groups on the 2H–MoS_2 surface results in similar electronic band structures. When we compare these band structures to those of pure 2H–MoS_2, we observe a significant modification: there is an in-gap state at the Fermi level, which is shifted to the bottom of the CB. During functionalization of the 1T-phase, the electronic band structures reveal electron conducting behavior as well as three additional energy levels in the CB region caused by the functional group (see Fig. 9). Overall, we can observe that the band structures of the four 1T-MoS_2 cases are similar, meaning that the band state is not the main reason for the differences in the HER behaviors of the four different functionalized MoS_2 samples.

To understand the ligand effect, we investigated the adsorption of one/two water molecules on each of the functionalized MoS_2 surfaces. In the structural optimizations, the water molecules were placed approximately 2.23–2.36 Å from the S layer. Subsequently, the adsorption energies of the water were calculated as the total energy difference between the product and reactant sides. According to the results in Table 1, water does not preferentially adsorb on the 2H–MoS_2 surface *via*

Table 1 Calculated adsorption energies of the adsorption of one and two water molecules on the functionalized MoS_2 surface

E_{ads} (eV)		f(ME)–MoS_2	f(COOH)–MoS_2	f(OME)–MoS_2	f(OH)–MoS_2
2H phase	One H_2O	−0.07	0.01	−0.05	−0.04
	Two H_2O	−0.02	0.25	−0.07	−0.21
1T phase	One H_2O	0.01	0.01	−0.06	−0.24
	Two H_2O	0.05	−0.11	−0.20	−0.27

phenyl–COOH functionalization. In the other three 2H–MoS_2 samples, we observe that H_2O can establish weak van der Waals interactions with the S atoms on the surface, with adsorption energies of −0.21 to −0.02 eV. For the 1T-MoS_2 phase, phenyl-ME functionalization is repulsive to water. Interestingly, phenyl–COOH functionalization is quite repulsive to one water molecule (0.01 eV) but attractive to two water molecules (−0.11 eV). From the overall calculation, we determine that the best performance of COOH-functionalized MoS_2 is produced by a combination of effects, such as the various ΔG_H quantities, number of active sites, and wettability values.

Discussion

To clearly investigate the effects of wettability and intramolecular proton transfer, we conducted in situ HER measurements on a Au electrode with a self-assembled monolayer composed of organic molecules. If the organic molecules do not participate in HER, a current drop will occur in a similar bias voltage range because the Au electrode is passivated by the organic molecules and the organic molecules cannot change the Fermi level of Au. The ME and OME self-assembled Au electrodes present an upshift in the reaction potential, while the OH and COOH self-assembled Au electrodes demonstrate a downshift in the reaction potential to even lower than that of the bare Au electrode (Fig. 7b). This suggests that the COOH and OH self-assembled Au electrodes not only increase the polarizability of the electrode but also affect the Gibbs free energy of the intermediate state during the HER. The reduction potential of the reaction decreases as the density of the organic molecules increases, facilitating the HER performance (Fig. 7a). To understand the separate effects of wettability and intramolecular proton transfer, we also conducted HER measurements with NO_2 and NH_2 self-assembled layers (Fig. 7d). Both of the surfaces with NO_2 and NH_2 functional groups are highly hydrophilic, but no intramolecular proton transfer occurs. As we know, the NO_2 group has no H molecules but has a large polarity. Hence, the NH_2 group has very high H dissociation energy and low polarity. Both of the organic self-assembled layers demonstrate a much higher reaction potential than the COOH-assembled and OH-assembled Au or even bare Au, which means that intramolecular proton transfer occurs in the COOH and OH functional groups during the HER. As a result, the electrochemistry of the HER in our system avoids energy-wasting reactions while coupling the proton-accepting or proton-donating groups in the MoS_2 catalyst[44].

Finally, we examined the HER performance of other important catalysts, including molecularly functionalized $MoTe_2$ and graphene. The polarization curves of the current density-potential characteristics suggest that the HER activities of molecularly functionalized $MoTe_2$ (f(COOH)–$MoTe_2$) and graphene (f(COOH)–CVDg) are enhanced (Fig. 10a). The onset potential of f(COOH)–$MoTe_2$ is reduced from 115 to 79 mV. The Tafel slope also decreases from 150 mV per decade to 118 mV per decade. In addition, the catalytic activity of f(COOH)–CVDg is improved. CVD graphene does not show a significant catalytic effect without any modification; however, f(COOH)–CVDg shows a good overpotential of approximately 82 mV and a Tafel slope of approximately 95 mV per decade (Fig. 10b). Even without any metal components or Au conductor, the molecularly functionalized graphene electrode shows a good onset potential (100 mV). This is the best onset potential without any metal incorporation or metal conductor (Fig. 11 and S14). As a result, we can conclude that the f(COOH)–CVDg electrode facilitates the HER catalytic effect with a help of intramolecular proton transfer in the functionalized organic molecules. Unlike the HER performance for MoS_2, relatively high Tafel slopes are observed for both functionalized $MoTe_2$ and graphene. However, we do not know the exact reason why the Tafel slopes of f(COOH)–CVDg and f(COOH)–$MoTe_2$ are higher than that of f-MoS_2; more experimental optimization and research are needed in the future.

In this study, we suggest a new pathway to enhance the electrocatalytic effect of 2D materials with four different functional molecules, including phenyl–Me,

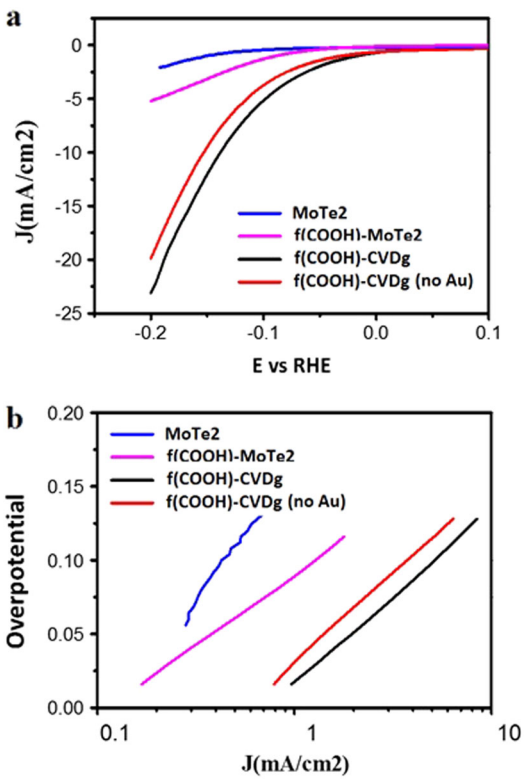

Fig. 10 Electrochemical measurements used to determine the effect of functionalization: a J–V curves and **b** corresponding Tafel slopes of bare $MoTe_2$ on a Au conductor ($MoTe_2$), COOH-functionalized $MoTe_2$ on a Au conductor (f-$MoTe_2$), COOH-functionalized CVD graphene on a Au conductor (fg_CVD), and COOH-functionalized CVD graphene on a plastic substrate (fg_CVD no Au)

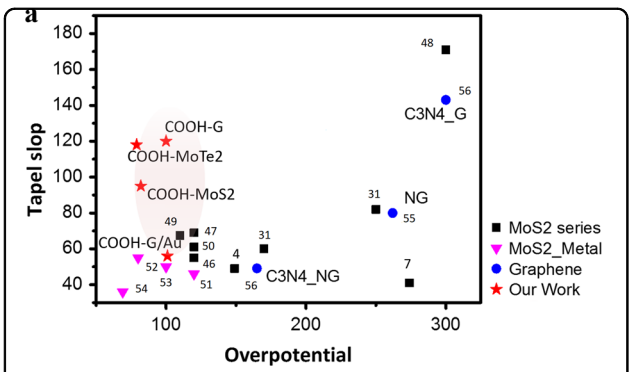

Fig. 11 a Trend plots of overpotentials and Tafel slopes from previous work, including those for modified MoS_2 (black), metal-incorporated MoS_2 (pink), modified graphene (blue), and the samples in our work (red)[46–56]

phenyl–OMe, phenyl–OH, and phenyl–COOH. The acidic molecular functionalization of MoS_2 materials not only reduces the onset potential and Tafel slope but also increases the device stability during the HER. Without any metal components, highly efficient catalytic effects were demonstrated. These effects are caused by an increase in the carrier density near the Fermi level and represent a new pathway to engineer both the hydrogen adsorption and desorption energy. Moreover, the phenyl–COOH functional group improves the HER catalytic effect of $MoTe_2$, which is another TMD material. In addition, f(COOH)–CVDg, which is another 2D carbon material without metal incorporation, produces a high-performance HER electrode. The best HER performance of the COOH-functionalized active materials is attributed to both the higher carrier concentration and the lower H desorption energy driven by intramolecular proton transfer. In our study, it was shown that 2D nanosheets with organic molecular functional groups experience different chemistries than the corresponding bulk or surface chemistry[45]; thus, the catalytic effect of TMD materials should be studied because the quantum chemical modulation of 2D TMD materials has yet to be researched in detail, despite their large potential in various bulk devices. Our results encourage new strategies for the chemical, electronic, and electrochemical modulation of 2D materials. The methodology developed in this study can be applied to other types of nano-dimensional materials in addition to 2D materials.

Acknowledgements
This work was supported by IBS-R011-D1. This work was supported by the Postdoctoral Research Program of Sungkyunkwan University (2017).

Author details
[1]Department of Energy Science, Sungkyunkwan University, Suwon 440-746, Korea. [2]Department of Engineering, Cambridge Graphene Center, University of Cambridge, Cambridge CB3 0FA, UK. [3]Center for Integrated Nanostructure Physics, Institute for Basic Science (IBS), Sungkyunkwan University, Suwon 440-746, Korea. [4]Department of Chemistry, Sungkyunkwan University, Suwon 440-746, Korea. [5]Center for Innovative Materials and Architectures (INOMAR), Vietnam National University-Ho Chi Minh City (VNU-HCM), Ho Chi Minh City, 721337 Vietnam, USA

Conflict of interest
The authors declare that they have no conflict of interest.

Supplementary information is available for this paper at https://doi.org/10.1038/s41427-018-0037-2.

Received: 20 October 2017 Revised: 7 February 2018 Accepted: 12 February 2018.
Published online: 24 May 2018

References

1. Li, W., Liu, J. & Zhao, D. Mesoporous materials for energy conversion and storage devices. *Nat. Rev. Mater.* **1**, 16023 (2016).
2. Pinhassi, R. I. et al. Hybrid bio-photo-electro-chemical cells for solar water splitting. *Nat. Commun.* **7**, 12552 (2016).

3. Mistry, H., Varela, A. S., Kühl, S., Strasser, P. & Cuenya, B. R. Nanostructured electrocatalysts with tunable activity and selectivity. *Nat. Rev. Mater.* **1**, 16009 (2016).
4. Gao, M.-R., Chan, M. K. Y. & Sun, Y. Edge-terminated molybdenum disulfide with a 9.4-Å interlayer spacing for electrochemical hydrogen production. *Nat. Commun.* **6**, 7493 (2015).
5. Voiry, D. et al. Conducting MoS2 nanosheets as catalysts for hydrogen evolution reaction. *Nano Lett.* **13**, 6222–6227 (2013).
6. Cummins, D. R. et al. Efficient hydrogen evolution in transition metal dichalcogenides via a simple one-step hydrazine reaction. *Nat. Commun.* **7**, 11857 (2016).
7. Geng, X. et al. Pure and stable metallic phase molybdenum disulfide nanosheets for hydrogen evolution reaction. *Nat. Commun.* **7**, 10672 (2016).
8. Voiry, D. et al. The role of electronic coupling between substrate and 2D MoS2 nanosheets in electrocatalytic production of hydrogen. *Nat. Mater.* **15**, 1003–1009 (2016).
9. Butler, S. Z. et al. Progress, challenges, and opportunities in two-dimensional materials beyond graphene. *ACS Nano* **7**, 2898–2926 (2013).
10. Lee, H., Kim, I., Kim, M. & Lee, H. Moving beyond flexible to stretchable conductive electrodes using metal nanowires and graphenes. *Nanoscale* **8**, 1789–1822 (2016).
11. Wang, H., Yuan, H., Sae Hong, S., Li, Y. & Cui, Y. Physical and chemical tuning of two-dimensional transition metal dichalcogenides. *Chem. Soc. Rev.* **44**, 2664–2680 (2015).
12. Conway, B. E. & Tilak, B. V. Interfacial processes involving electrocatalytic evolution and oxidation of H2, and the role of chemisorbed H. *Electrochim. Acta* **47**, 3571–3594 (2002).
13. Wang, J. et al. Field effect enhanced hydrogen evolution reaction of MoS2 nanosheets. *Adv. Mater.* **29**, 1604464–n/a (2017).
14. Niu, F. et al. A novel hybrid artificial photosynthesis system using MoS2 embedded in carbon nanofibers as electron relay and hydrogen evolution catalyst. *J. Catal.* **352**, 35–41 (2017).
15. Voiry, D., Yang, J. & Chhowalla, M. Recent strategies for improving the catalytic activity of 2D TMD nanosheets toward the hydrogen evolution reaction. *Adv. Mater.* **28**, 6197–6206 (2016).
16. Roubelakis, M. M., Bediako, D. K., Dogutan, D. K. & Nocera, D. G. Proton-coupled electron transfer kinetics for the hydrogen evolution reaction of hangman porphyrins. *Energy Environ. Sci.* **5**, 7737–7740 (2012).
17. Li, Y., Xu, C.-Y. & Zhen, L. Surface potential and interlayer screening effects of few-layer MoS2 nanoflakes. *Appl. Phys. Lett.* **102**, 143110 (2013).
18. Lee, H. et al. Highly efficient thin-film transistor via cross-linking of 1T edge functional 2H molybdenum disulfides. *ACS Nano* **11**, 12832–12839 (2017).
19. Wang, H., Lu, Z., Xu, S., Kong, D., Cha, J. J. & Zheng, G. et al. Electrochemical tuning of vertically aligned MoS2 nanofilms and its application in improving hydrogen evolution reaction. *Proc. Natl. Acad. Sci.* **110**, 19701–19706 (2013).
20. Lukowski, M. A., Daniel, A. S., Meng, F., Forticaux, A., Li, L. & Jin, S. Enhanced hydrogen evolution catalysis from chemically exfoliated metallic MoS2 nanosheets. *J. Am. Chem. Soc.* **135**, 10274–10277 (2013).
21. Yu, Y., Huang, S.-Y., Li, Y., Steinmann, S. N., Yang, W. & Cao, L. Layer-dependent electrocatalysis of MoS2 for hydrogen evolution. *Nano. Lett.* **14**, 553–558 (2014).
22. Chakraborty, B., Matte, H. S. S. R., Sood, A. K. & Rao, C. N. R. Layer-dependent resonant Raman scattering of a few layer MoS2. *J. Raman Spectrosc.* **44**, 92–96 (2013).
23. Zheng, Y., Jiao, Y., Jaroniec, M. & Qiao, S. Z. Advancing the electrochemistry of the hydrogen-evolution reaction through combining experiment and theory. *Angew. Chem. Int. Ed.* **54**, 52–65 (2015).
24. Zhu, L. et al. A rhodium/silicon co-electrocatalyst design concept to surpass platinum hydrogen evolution activity at high overpotentials. *Nat. Commun.* **7**, 12272 (2016).
25. Kiriya, D., Tosun, M., Zhao, P., Kang, J. S. & Javey, A. Air-Stable surface charge transfer doping of MoS2 by benzyl viologen. *J. Am. Chem. Soc.* **136**, 7853–7856 (2014).
26. Backes, C. et al. Functionalization of liquid-exfoliated two-dimensional 2H-MoS2. *Angew. Chem. Int. Ed.* **54**, 2638–2642 (2015).
27. Yang, X., Meng, N., Zhu, Y., Zhou, Y., Nie, W. & Chen, P. Greatly improved mechanical and thermal properties of chitosan by carboxyl-functionalized MoS2 nanosheets. *J. Mater. Sci.* **51**, 1344–1353 (2016).
28. Chakraborty, B., Bera, A., DVS, Muthu, Bhowmick, S., Waghmare, U. V. & Sood, A. K. Symmetry-dependent phonon renormalization in monolayer MoS2 transistor. *Phys. Rev. B* **85**, 161403 (2012).
29. Alexeev, A., Loos, J. & Koetse, M. M. Nanoscale electrical characterization of semiconducting polymer blends by conductive atomic force microscopy (C-AFM). *Ultramicroscopy* **106**, 191–199 (2006).
30. Chen, Z., Cummins, D., Reinecke, B. N., Clark, E., Sunkara, M. K. & Jaramillo, T. F. Core–shell MoO3–MoS2 nanowires for hydrogen evolution: a functional design for electrocatalytic materials. *Nano Lett.* **11**, 4168–4175 (2011).
31. Li, H. et al. Activating and optimizing MoS2 basal planes for hydrogen evolution through the formation of strained sulphur vacancies. *Nat. Mater.* **15**, 48–53 (2016).
32. Bhardwaj, M. & Balasubramaniam, R. Uncoupled non-linear equations method for determining kinetic parameters in case of hydrogen evolution reaction following Volmer–Heyrovsky–Tafel mechanism and Volmer–Heyrovsky mechanism. *Int. J. Hydrogen Energy* **33**, 2178–2188 (2008).
33. Knowles, J. R. & Jencks, W. P. The intrinsic PkA-values of functional groups in enzymes: improper deductions from the Ph-dependence of steady-state parameter. *Crit. Rev. Biochem.* **4**, 165–173 (1976).
34. Costentin, C., Robert, M. & Savéant, J.-M. Electrochemical concerted proton and electron transfers. Potential-dependent rate constant, reorganization factors, proton tunneling and isotope effects. *J. Electroanal. Chem.* **588**, 197–206 (2006).
35. Hohenberg, P. & Kohn, W. Inhomogeneous electron gas. *Phys. Rev.* **136**, B864–B71 (1964).
36. Kohn, W. & Sham, L. J. Self-consistent equations including exchange and correlation effects. *Phys. Rev.* **140**, A1133–A1138 (1965).
37. Kresse, G. & Furthmüller, J. Efficiency of ab-initio total energy calculations for metals and semiconductors using a plane-wave basis set. *Comput. Mater. Sci.* **6**, 15–50 (1996).
38. Kresse, G. & Furthmüller, J. Efficient iterative schemes forab initiototal-energy calculations using a plane-wave basis set. *Phys. Rev. B* **54**, 11169–86 (1996).
39. Blöchl, P. E. Projector augmented-wave method. *Phys. Rev. B* **50**, 17953–79 (1994).
40. Perdew, J. P., Parr, R. G., Levy, M. & Balduz, J. L density-functional theory for fractional particle number: derivative discontinuities of the energy. *Phys. Rev. Lett.* **49**, 1691–4 (1982).
41. Grimme, S., Antony, J., Ehrlich, S. & Krieg, H. A consistent and accurate ab initio parametrization of density functional dispersion correction (DFT-D) for the 94 elements H–Pu. *J. Chem. Phys.* **132**, 154104 (2010).
42. Ouyang, Y., Ling, C., Chen, Q., Wang, Z., & Shi, L. Wang Activating inert basal planes of MoS2 for hydrogen evolution reaction through the formation of different intrinsic defects. *J. Chem. Mater.* **28**, 4390–4396 (2016).
43. Tang, Q. & Jiang, D. –E. Mechanism of hydrogen evolution reaction on 1T MoS2 from first principles. *ACS Catal.* **6**, 4953–4961 (2016).
44. Rosenthal, J. & Nocera, D. G. Role of proton-coupled electron transfer in O–O bond activation. *Acc. Chem. Res.* **40**, 543–553 (2007).
45. Chen, X. & McDonald, A. R. Functionalization of two-dimensional transition-metal dichalcogenides. *Adv. Mater.* **28**, 5738–5746 (2016).
46. Wang, F. Z. et al. Ammonia intercalated flower-like MoS2 nanosheet film as electrocatalyst for high efficient and stable hydrogen evolution. *Sci. Rep.* **6**, 31092 (2016).
47. Xu, S., Li, D. & Wu, P. One-pot, facile, and versatile synthesis of monolayer MoS2/WS2 quantum dots as bioimaging probes and efficient electrocatalysts for hydrogen evolution reaction. *Adv. Funct. Mater.* **25**, 1127–1136 (2015).
48. Ye, G., Gong, Y., Lin, J., Li, B., He, Y. & Pantelides, S. T. et al. Defects engineered monolayer MoS2 for improved hydrogen evolution reaction. *Nano Lett.* **16**, 1097–1103 (2016).
49. Ma, L. et al. In situ thermal synthesis of inlaid ultrathin MoS2/graphene nanosheets as electrocatalysts for the hydrogen evolution reaction. *Chem. Mater.* **28**, 5733–5742 (2016).
50. Jiang, Y., Li, X., Yu, S., Jia, L., Zhao, X. & Wang, C. Reduced graphene oxide-modified carbon nanotube/polyimide film supported MoS2 nanoparticles for electrocatalytic hydrogen evolution. *Adv. Funct. Mater.* **25**, 2693–2700 (2015).
51. Wang, D.-Y. et al. Highly active and stable hybrid catalyst of cobalt-doped FeS2 nanosheets–carbon nanotubes for hydrogen evolution reaction. *J. Am. Chem. Soc.* **137**, 1587–1592 (2015).
52. Gong, Q. et al. Ultrathin MoS2(1–x)Se2x alloy nanoflakes for electrocatalytic hydrogen evolution reaction. *ACS Catal.* **5**, 2213–2219 (2015).
53. Cummins, D. R. et al. Catalytic activity in lithium-treated core–shell MoOx/MoS2 nanowires. *J. Phys. Chem. C* **119**, 22908–22914 (2015).

54. Dai, X. et al. Co-doped MoS2 nanosheets with the dominant CoMoS phase coated on carbon as an excellent electrocatalyst for hydrogen evolution. *ACS Appl. Mater. Interfaces* **7**, 27242–27253 (2015).
55. Yang, Y., Lun, Z., Xia, G., Zheng, F., He, M. & Chen, Q. Non-precious alloy encapsulated in nitrogen-doped graphene layers derived from MOFs as an active and durable hydrogen evolution reaction catalyst. *Energy Environ. Sci.* **8**, 3563–3571 (2015).
56. Duan, J., Chen, S., Jaroniec, M. & Qiao, S. Z. Porous C3N4 nanolayers@N-graphene films as catalyst electrodes for highly efficient hydrogen evolution. *ACS Nano* **9**, 931–940 (2015).